PNAS RESEARCH ARTICLE | IMMUNOLOGY AND INFLAMMATION

A mouse model to distinguish NLRP6-mediated inflammasome-dependent and -independent functions

Runzhi Li[a,b,1], Yang Zan[a,b,1], Decai Wang[b,c], Xuequn Chen[a,b], Anmin Wang[a,b], Haoyuan Tan[a,b], Guorong Zhang[a,b], Siyuan Ding[d], Chen Shen[e,2], Hao Wu[f,g,2], and Shu Zhu[a,b,c,2]

Contributed by Hao Wu; received December 6, 2023; accepted December 28, 2023; reviewed by Bo Hu and Jie Zheng

The NOD-like receptor (NLR) family pyrin domain containing 6 (NLRP6) serves as a sensor for microbial dsRNA or lipoteichoic acid (LTA) in intestinal epithelial cells (IECs), and initiating multiple pathways including inflammasome pathway and type I interferon (IFN) pathway, or regulating nuclear factor-κB (NF-κB) and mitogen-activated protein kinase (MAPK) pathways. NLRP6 can exert its function in both inflammasome-dependent and inflammasome-independent manners. However, there is no tool to distinguish the contribution of individual NLRP6-mediated pathway to the physiology and pathology in vivo. Here, we validated that Arg39 and Trp50 residues in the pyrin domain (PYD) of murine NLRP6 are required for ASC recruitment and inflammasome activation, but are not important for the RNA binding and PYD-independent NLRP6 oligomerization. We further generated the *Nlrp6*$^{R39E\&W50E}$ mutant mice, which showed reduced inflammasome activation in either steady state intestine or during viral infection. However, the type I IFN production in cells or intestine tissue from *Nlrp6*$^{R39E\&W50E}$ mutant mice remain normal. Interestingly, NLRP6-mediated inflammasome activation or the IFN-I production seems to play distinct roles in the defense responses against different types of RNA viruses. Our work generated a useful tool to study the inflammasome-dependent role of NLRP6 in vivo, which might help to understand the complexity of multiple pathways mediated by NLRP6 in response to the complicated and dynamic environmental cues in the intestine.

NLRP6 | inflammasome | interferon | RNA virus | R39/W50 mutations

Significance

NLRP6 is an IEC-specific NLR that senses microbial dsRNA and LTA, which mediates inflammasome and type I IFN activation and may regulate NF-κB and MAPK pathways. Previous studies used complete knock-out of NLRP6 in mice to study its in vivo function, which cannot distinguish the multiple pathways mediated by NLRP6. Here, we generated a mutant mouse model by knocking in the R39E and W50E mutations to specifically block NLRP6-mediated inflammasome activation, which could distinguish inflammasome-dependent and -independent functions of NLRP6 in vivo.

NLRP6, a member of the NLR (nucleotide-oligomerization domain-like receptor) family, surveys the cytosolic compartment of cells for the detection of pathogen-associated molecular patterns (PAMPs) or damage-associated molecular patterns (DAMPs) (1, 2). NLRs exhibit a conserved domain organization, featuring the central nucleotide-binding domain (NBD), also known as the NACHT domain, the C-terminal leucine-rich repeats (LRRs), and an N-terminal effector domain [caspase activation and recruitment domain (CARD) or the pyrin domain (PYD)] (3, 4). In NLRP6, the NACHT domain and LRRs likely function in oligomerization and ligand binding, and its N-terminal PYD serves as the effector domain for inflammasome formation and activation.

NLRP6 shows preferential expression in specialized epithelial cells such as enterocytes and goblet cells within the intestinal tract (5–7). It plays a pivotal role in monitoring the microbial infection and regulating intestinal homeostasis through the inflammasome pathway, interferon (IFN) signaling, and regulation of nuclear factor-κB (NF-κB) and mitogen-activated protein kinase (MAPK) signaling (6–11). Initial observations in *Nlrp6*$^{-/-}$ mice under steady-state condition and after DSS-induced colitis revealed reduced inflammasome formation and serum IL-18 levels compared to wild-type (WT) control mice(6). Biochemical evidence supported this conclusion, showing that co-expression of NLRP6 and ASC results in caspase-1 activation and IL-18 secretion (9).

Besides the inflammasome pathway, NLRP6 is closely linked to the IFN-I pathway in response to viral infections (10). NLRP6 engages with the DEAH-box helicase 15 (DHX15), establishing a viral sensing complex that recognizes cytosolic long double-stranded RNA (dsRNA) and activates the mitochondrial antiviral signaling protein (MAVS) to induce interferon and interferon-stimulated genes (ISGs) (10). Our previous research also found that virus-derived dsRNA promotes NLRP6 liquid–liquid phase separation (LLPS), resulting in NLRP6 inflammasome activation (12). Despite serving as a hub with multiple roles in antiviral responses, the relative contributions of these NLRP6-mdediated pathways remain unclear.

Recent published cryo-electron microscopy (cryo-EM) structure of NLRP6 showed the filamentous assembly of NLRP6 pyrin domain, indicating its capability to form inflammasome machinery (13, 14). Notably, NLRP6^{PYD} can nucleate ASC^{PYD} more easily than NLRP3^{PYD} (14, 15). Additionally, two key amino acid residues (R42/W53) in human

Author contributions: R.L., Y.Z., C.S., H.W., and S.Z. designed research; R.L. and Y.Z. performed research; D.W., X.C., A.W., H.T., G.Z., and S.D. contributed new reagents/analytic tools; R.L. and Y.Z. analyzed data; D.W. and X.C. helped with cellular experiments; A.W. and H.T. helped with virus infection experiments; G.Z., S.D., and C.S. providing critical comments and suggestions; H.W. and S.Z. supervised the project; and R.L. and Y.Z. wrote the paper with input from all authors.

Reviewers: B.H., St. Jude Children's Research Hospital; and J.Z., Shanghai Institute of Materia Medica Chinese Academy of Sciences.

The authors declare no competing interest.

[1]R.L. and Y.Z. contributed equally to this work.

[2]To whom correspondence may be addressed. Email: shenc@wustl.edu, wu@crystal.harvard.edu, or zhushu@ustc.edu.cn.

This article contains supporting information online at https://www.pnas.org/lookup/suppl/doi:10.1073/pnas.2321419121/-/DCSupplemental.

Published January 30, 2024.

NLRP6 are crucial for NLRP6^{PYD} filament formation, as confirmed through biochemical experiments (14). Here, we validated the homologs R39/W50 in mouse NLRP6 are essential for NLRP6 inflammasome activation by recruiting ASC in cells. Intriguingly, this mutant only interfered with ASC filament formation but did not affect the IFN-I pathway. Meanwhile, we generated the *Nlrp6*$^{R39E\&W50E}$ mutant mice and demonstrated that both NLRP6-dependent inflammasome activation and IFN-I production are pivotal components of NLRP6-mediated antivirus responses.

Results

Residues R39/W50 of NLRP6 Are Crucial for ASC Recruitment. A typical NLR inflammasome activation involves ligand recognition and the formation of oligomers through homotypic interactions with the adaptor Asc and the pro-inflammatory effector protease caspase-1 (14, 16, 17). To assess the impact of two residues R39/W50 in mouse NLRP6, we investigated key aspects of NLRP6 inflammasome assembly and the NLRP6-mediated IFN-I pathway in HEK293T cells (Fig. 1 *A* and *B*). Consistent with the previous report (14), R39/W50 are essential for interacting with ASC and subsequently ASC polymerization (Fig. 1 *C* and *D*). R42/W53 of human NLRP6 are also important for the interaction between NLRP6 and Asc (*SI Appendix*, Fig. S1 *A* and *B*). However, the R39E&W50E mutation had no impact on dsRNA recognition by NLRP6 (Fig. 1*E*) or oligomerization (Fig. 1*F*). Based on the cryo-EM structure of NLRP6^{PYD} filament, it was speculated that the assembly of the NLRP6 inflammasome undergoes two nucleation-induced polymerization steps. First, oligomeric NLRP6 nucleates ASC filaments via homotypic PYD–PYD interactions, resulting in ASC aggregation. Second, polymerized ASC acts as a nucleation site for caspase-1 filaments through CARD–CARD interactions, resulting in the activation of caspase-1 (14). Our findings demonstrate that the R39E&W50E mutation effectively inhibited ASC polymerization by disrupting the PYD–PYD interaction, underscoring the significance of the R39/W50 sites in NLRP6 inflammasome assembly. To investigate whether the R39E&W50E mutation affects the IFN-I pathway triggered by NLRP6, we examined two crucial partners in NLRP6-dependent IFN-I signaling, namely DHX15 and MAVS. Interestingly, the R39E&W50E mutation had no impact on the interaction with DHX15 or MAVS (Fig. 1 *G* and *H*). In summary, these data suggest that R39/W50 of NLRP6 are crucial for ASC recruitment and polymerization, while not affecting the sensing and oligomerization of NLRP6 itself, as well as its interaction with DHX15 or MAVS.

NLRP6$^{R39E\&W50E}$ Does Not Support Inflammasome Activation in Cells. NLRP6 recruits ASC and caspase-1 to form an inflammasome complex, cleaving IL-18 into their biologically active forms and GSDMD to induce pyroptosis (3, 18). To determine the downstream effects of the R39E&W50E mutation, we examined caspase-1 activation and GSDMD cleavage in a reconstruction system in HEK293T cells. Notably, NLRP6$^{R39E\&W50E}$ completely impaired the cleavages of GSDMD and caspase-1 (Fig. 2*A* and *SI Appendix*, Fig. S2*A*). In consistency, overexpression of NLRP6$^{R39E\&W50E}$ resulted in reduced ballooning of the cell membrane, decreased propidium iodide (PI) influx, and lowered lactate dehydrogenase (LDH) release compared to WT-NLRP6 (Fig. 2 *B–E* and *SI Appendix*, Fig. S2 *B–E*). NLRP6 and ASC form puncta in cells (8, 19, 20). Thus, we generated HEK293T cells stably co-expressing NLRP6–GFP and ASC–mCherry and found that NLRP6$^{R39E\&W50E}$ exhibited markedly reduced NLRP6–ASC puncta formation (Fig. 2 *F* and *G*). In previous studies, we established that immortalized mouse bone marrow-derived macrophages (iBMDMs) stably express NLRP6, inducing spontaneous activation of the inflammasome and cell death, providing a valuable model for studying the underlying mechanisms of NLRP6 inflammasome activation (12). In iBMDMs reconstituted with NLRP6$^{R39E\&W50E}$ mutant, we observed that the mutant could not activate the NLRP6 inflammasome, as evidenced by dramatically decreased cleavages of caspase-1 and GSDMD, PI staining, LDH release, and ballooning morphology (Fig. 2 *H–L*). Collectively, these data suggest that NLRP6$^{R39E\&W50E}$ indeed cannot support NLRP6 inflammasome activation, providing a foundation for subsequent functional studies in mice.

R39/W50 of NLRP6 Are Required for NLRP6 Inflammasome Activation In Vivo. To test the physiological role of NLRP6$^{R39E\&W50E}$ in vivo, we generated mutant mice carrying the R39E&W50E mutation in *Nlrp6* by CRISPR knock-in strategy (Fig. 3*A*). Consistent with aforementioned observations in vitro, the expression of NLRP6 in *Nlrp6*$^{R39E\&W50E}$ mice was not affected and the R39E&W50E mutation did not affect NLRP6 oligomerization (Fig. 3*B*). Next, we detected the downstream effects of the NLRP6 inflammasome in the intestines of *Nlrp6*$^{R39E\&W50E}$, *Nlrp6*$^{-/-}$, and WT mice. The intestinal explants in jejunum or ileum from both *Nlrp6*$^{R39E\&W50E}$mice and *Nlrp6*$^{-/-}$ mice showed decreased GSDMD cleavage compared to those from WT mice (Fig. 3 *C* and *D*). These explants from both *Nlrp6*$^{R39E\&W50E}$mice and *Nlrp6*$^{-/-}$ mice also produce much less IL-18 than those from WT mice (Fig. 3*E*). Recalling the previous studies in which we found a reduction in GSDMD cleavage and a decrease in IL-18 secretion following NLRP6 deficiency (12), the *Nlrp6*$^{R39E\&W50E}$mutant mice showed similar phenotype with *Nlrp6*$^{-/-}$ mice in terms of the steady-state inflammasome activation in the intestine.

Both NLRP6-Mediated Inflammasome Activation and IFN-I Production Are Important for the Restriction of Virus Infection in Cells. Previous study showed that NLRP6 recognizes viral RNA together with DHX15 and recruits MAVS to regulate the production of IFN-I and ISGs, in response to the virus infection (10). Given that the R39E&W50E mutation has no effect on the binding of NLRP6 to DHX15 or MAVS (Fig. 1 *G* and *H*), we speculated that the R39E&W50E mutation does not impact the NLRP6-mediated IFN-I pathway, making it a perfect tool to evaluate the potential roles of NLRP6-induced inflammasome and IFN-I pathways during virus infection. To test the pathological role of NLRP6$^{R39E\&W50E}$, we used three different RNA viruses, rotavirus (RV), encephalomyocarditis virus (EMCV), and vesicular stomatitis virus (VSV), to infect intestinal organoids or primary mouse embryonic fibroblasts (MEFs) derived from *Nlrp6*$^{-/-}$, *Nlrp6*$^{R39E\&W50E}$, or WT mice (Fig. 4*A*). Interestingly, we found that the *Nlrp6*$^{R39E\&W50E}$ mice is able to control virus infection better than *Nlrp6*$^{-/-}$ mice when dealing with RV and EMCV but is not as good as WT mice when dealing with RV and VSV (Fig. 4 *B-G*). We then measured the interferon and ISGs in MEFs derived from *Nlrp6*$^{-/-}$, *Nlrp6*$^{R39E\&W50E}$, or WT mice inducted by three viruses. Notably, while NLRP6 deficiency affects the IFN-I production during early infection (Fig. 4 *H–S*), in most cases, R39E&W50E mutation did not affect the production of IFN-β and various ISGs during virus infection in comparison to WT MEFs (Fig. 4 *H–S*), however, during EMCV infection, the expression of *Ifnb* and *Oas1a* were significantly higher in *Nlrp6*$^{R39E\&W50E}$ MEFs than in WT MEFs (Fig. 4 *H–S*), indicating the existence of potential compensatory elevation of IFN-I pathway due to the blockade of inflammasome pathway. Together, these data suggest

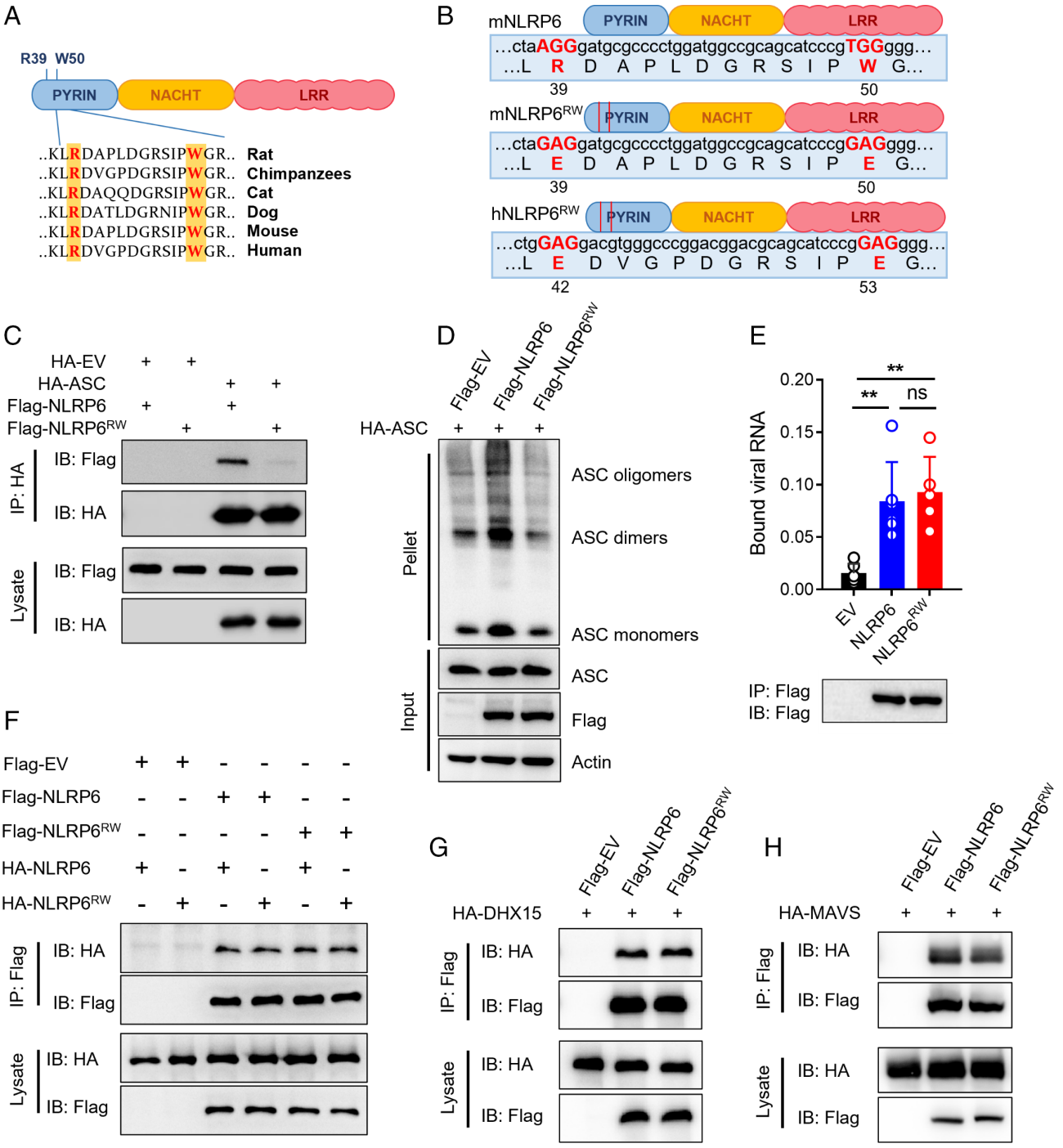

Fig. 1. The NLRP6$^{R39E\&W50E}$ (NLRP6^{RW}) mutation interrupts the interaction between NLRP6 and ASC but does not affect the binding of NLRP6 with RNA or the oligomerization of NLRP6. (*A*) Conservation of R39/W50 sites of NLRP6 in different species, aligned using Mega X. (*B*) Schematic diagram of the R39E&W50E mutation of mouse NLRP6 (corresponding to the R42E&W53E mutation in human NLRP6). (*C*) Immunoprecipitation (IP) and western blot analysis to evaluate the NLRP6–ASC interaction in HEK293T cells transfected with expression vectors for various combinations (*Upper* lanes), followed by immunoprecipitation of lysates with anti-HA and immunoblot analysis with anti-HA and anti-Flag. (*D*) Western blot analysis of crosslinked ASCs in the NP-40–insoluble pellet of HEK293T cells transfected with different expression vectors. (*E*) qPCR of viral RNA bound by Flag-mNLRP6 and its mutant expressed in EMCV-infected HEK293T cells. (*F*) IP and western blot analysis to evaluate NLRP6 self-association in HEK293T cells transfected with expression vectors for various combinations (*Upper* lanes), followed by immunoprecipitation of lysates with anti-Flag and immunoblot analysis with anti-HA and anti-Flag. (*G*) IP and western blot analysis to evaluate the NLRP6–DHX15 interaction in the lysates of HEK293T cells overexpressed Flag-mNLRP6 or its mutant. (*H*) IP and western blot analysis to evaluate the NLRP6–MAVS interaction in the lysates of HEK293T cells overexpressed Flag-mNLRP6 or its mutant. Data are representative of at least three independent experiments. The results are shown as mean ± SD. $^{**}P < 0.01$; ns, not significant.

that both NLRP6-mediated inflammasome pathway and the NLRP6-mediated IFN-I pathway contribute to the antiviral immune responses. Moreover, our findings revealed distinct contributions of these two pathways to the antiviral defense against different viruses.

Both NLRP6-Mediated Inflammasome Activation and IFN-I Production Are Important for the Restriction of Virus Infection in Mice. To investigate the role of NLRP6$^{R39E\&W50E}$ in anti-virus response in vivo, we infected WT, *Nlrp6*$^{-/-}$, and *Nlrp6*$^{R39E\&W50E}$ mice with the rotavirus (RV) EC strain, which belongs to the

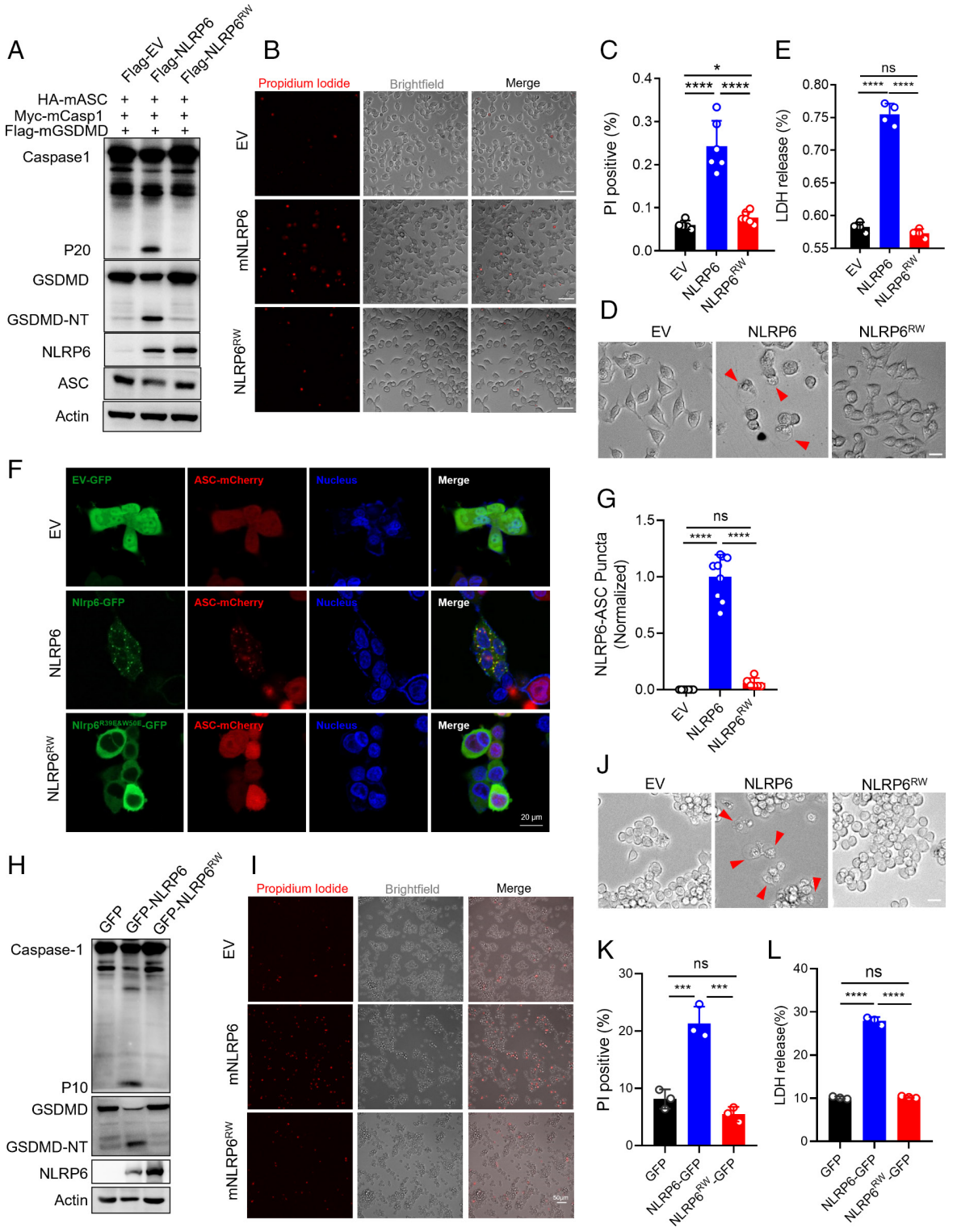

Fig. 2. The NLRP6^{RW} mutation suppresses the activation of NLRP6 inflammasome in cells. (*A–E*) show the NLRP6^{RW} mutation suppresses NLRP6 inflammasome activation in HEK293T cells. (*A*) Plasmids encoding HA-mASC, Myc-mCasp1, Flag-mGSDMD, Flag-mNLRP6, or its mutant were co-transfected into HEK293T cells for 24 h to reconstruct the NLRP6 inflammasome, followed by immunoblotting with antibodies against the indicated proteins. (*B*) Propidium Iodide (PI) staining of HEK293T cells overexpressed Flag-mNLRP6 or its mutant, and other NLRP6 inflammasome components including HA-mASC, Myc-mCasp1, and Flag-mGSDMD. (Scale bar, 50 μm.) In addition, (*C*) is the quantification of PI-positive cells. (*D*) Representative cell images (arrowheads indicate pyroptotic cells). (Scale bar, 20 μm.) (*E*) Pyroptotic cell death indicated by release of lactate dehydrogenase (LDH) in culture supernatants 24 h post transfected with NLRP6 or its mutant. (*F*) Representative images of NLRP6–ASC puncta in HEK293 cells 24 h post infection by NLRP6 or its mutant-containing lentiviruses. (Scale bar, 20 μm.) And (*G*) shows the quantification of puncta number. (*H–L*) show the NLRP6^{RW} mutation suppresses NLRP6 inflammasome activation in iBMDMs. (*H*) Immunoblots of GSDMD, Caspase-1, ASC, and Actin in iBMDMs transduced with lentiviruses expressing NLRP6 or its mutants. (*I*) PI staining of iBMDMs transduced with lentiviruses expressing NLRP6 or its mutants. (Scale bar, 50 μm.) In addition, (*K*) is the quantification of PI-positive cells. (*J*) Representative cell images (arrowheads indicate pyroptotic cells). (Scale bar, 20 μm.) (*L*) Pyroptotic cell death indicated by release of lactate dehydrogenase (LDH) in iBMDMs culture supernatants 24 h post transfected with NLRP6 or its mutant. Data are representative of at least three independent experiments. The results are shown as mean ± SD. *P < 0.05; **P < 0.01; ***P < 0.001; ****P < 0.0001; ns, not significant.

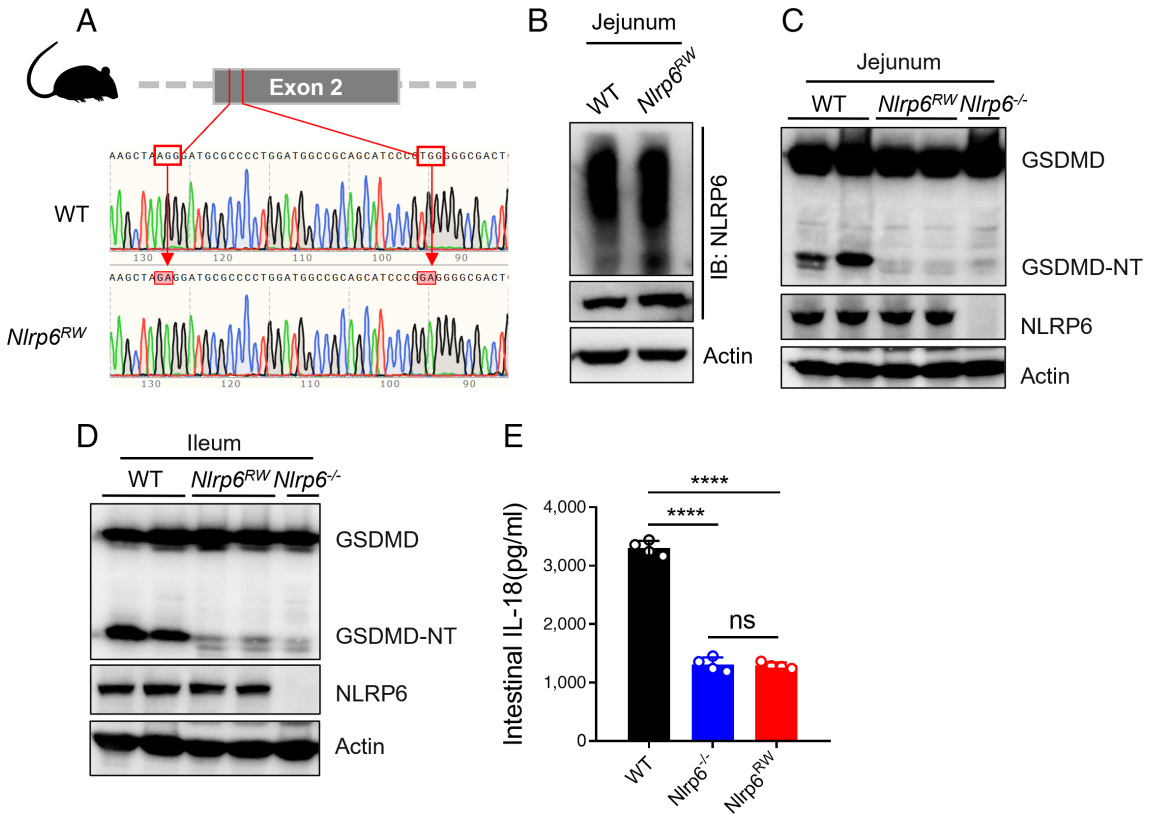

Fig. 3. The NLRP6^{RW} mutation suppresses NLRP6 inflammasome activation in mouse intestine under steady-state. (*A*) Generation strategy of *Nlrp6*^{RW} mutant mice. (*B*) Endogenous NLRP6 oligomerization in WT and *Nlrp6*^{RW} mice, assessed by SDD-AGE and IB with anti-NLRP6. WCLs were further analyzed by SDS-PAGE and probed by immunoblotting with anti-NLRP6 and anti-Actin. (*C* and *D*) Immunoblot of GSDMD, NLRP6, and Actin. Each lane is representative of jejunum (*C*) or ileum (*D*) tissues from an individual mouse. (*E*) Intestine-explant supernatant IL-18 levels determined by ELISA from WT, *Nlrp6*$^{-/-}$, and *Nlrp6*^{RW} mice. Data are representative of at least three independent experiments. The results are shown as mean ± SD. ****$P < 0.0001$; ns, not significant.

Reoviridae family (21) (Fig. 5*A*). We observed that *Nlrp6*$^{-/-}$ mice developed higher viral loads (Fig. 5*B*), underscoring the importance of NLRP6 in antiviral responses (10, 12). Additionally, we detected less IL-18 release in the supernatants and less GSDMD cleavage in the tissue of the jejunum explants of *Nlrp6*$^{R39E\&W50E}$ mice compared to those of WT mice during RV infection (Fig. 5 *C* and *D*), indicating impaired inflammasome activation due to the R39E&W50E mutation. Interestingly, we observed significantly enhanced viral replication in *Nlrp6*$^{R39E\&W50E}$ mice compared to WT mice, suggesting that inflammasome activation plays a crucial role in antiviral responses (Fig. 5*B*). Notably, we detected a reduced viral load in *Nlrp6*$^{R39E\&W50E}$ mice compared to *Nlrp6*$^{-/-}$ mice, indicating that NLRP6$^{R39E\&W50E}$-mediated IFN-I pathway still plays an antiviral role in anti-RV response (Fig. 5 *B* and *E–H*). Taken together, these data demonstrated that the R39E&W50E mutation specifically inhibits inflammasome activation without affecting the IFN-I pathway, resulting in partial retaining of antiviral responses, and dissected for the first time the differential contribution of the inflammasome and IFN-I pathways in NLRP6-mediated antiviral defense.

Discussion

NLRP6 plays essential roles in defending against pathogen infections and maintaining intestinal homeostasis (3, 22, 23). In the intestinal tract, NLRP6 is implicated in both inflammasome activation and inflammasome-independent functions, such as the IFN pathway, NF-κB pathway, and MAPK signaling (5–11, 19). Acting as a central regulator, NLRP6 orchestrates multiple pathways in complex pathological conditions (22). Our previous study revealed that viral dsRNA induces NLRP6 LLPS, serving as a central hub to regulate both inflammasome activation and the IFN-I pathway (12). Despite initiating different pathways through the recruitment of various adaptors, the relative contributions and precise mechanisms of NLRP6-mediated signaling pathways remain unknown. Our current work introduces a mouse model (*Nlrp6*$^{R39E\&W50E}$) capable of distinguishing between inflammasome-dependent and -independent functions of NLRP6 during viral infections. The R39/W50 residues are specifically required for the interaction between NLRP6 and ASC, without affecting IFN-I/ISG production (Fig. 4). This model provides valuable insights into the nuanced roles of NLRP6 in coordinating immune responses during viral infections.

Our understanding of the role of PRRs in recognizing and initiating responses to RNA virus invasions has expanded rapidly over the last decade (1, 24). To exert antiviral functions, PRRs induce the expression of type I and type III interferons, chemokines, and pro-inflammatory cytokines (24). IFNs play a crucial role as potent antiviral agents by promoting the expression of interferon-stimulated genes (ISGs) (25), which play an important role in antiviral defense by impeding viral entry, replication, and budding (26). The production of proinflammatory cytokines contributes to shaping the overall immune response by recruiting immune cells to the site of infection and activating adaptive immunity (27). NLRP6 has been shown to play dual roles in the intestinal antiviral response by forming inflammasome and activating DHX15-MAVS axis to mediate IFN production (10, 12). However, the different contributions of these two pathways in

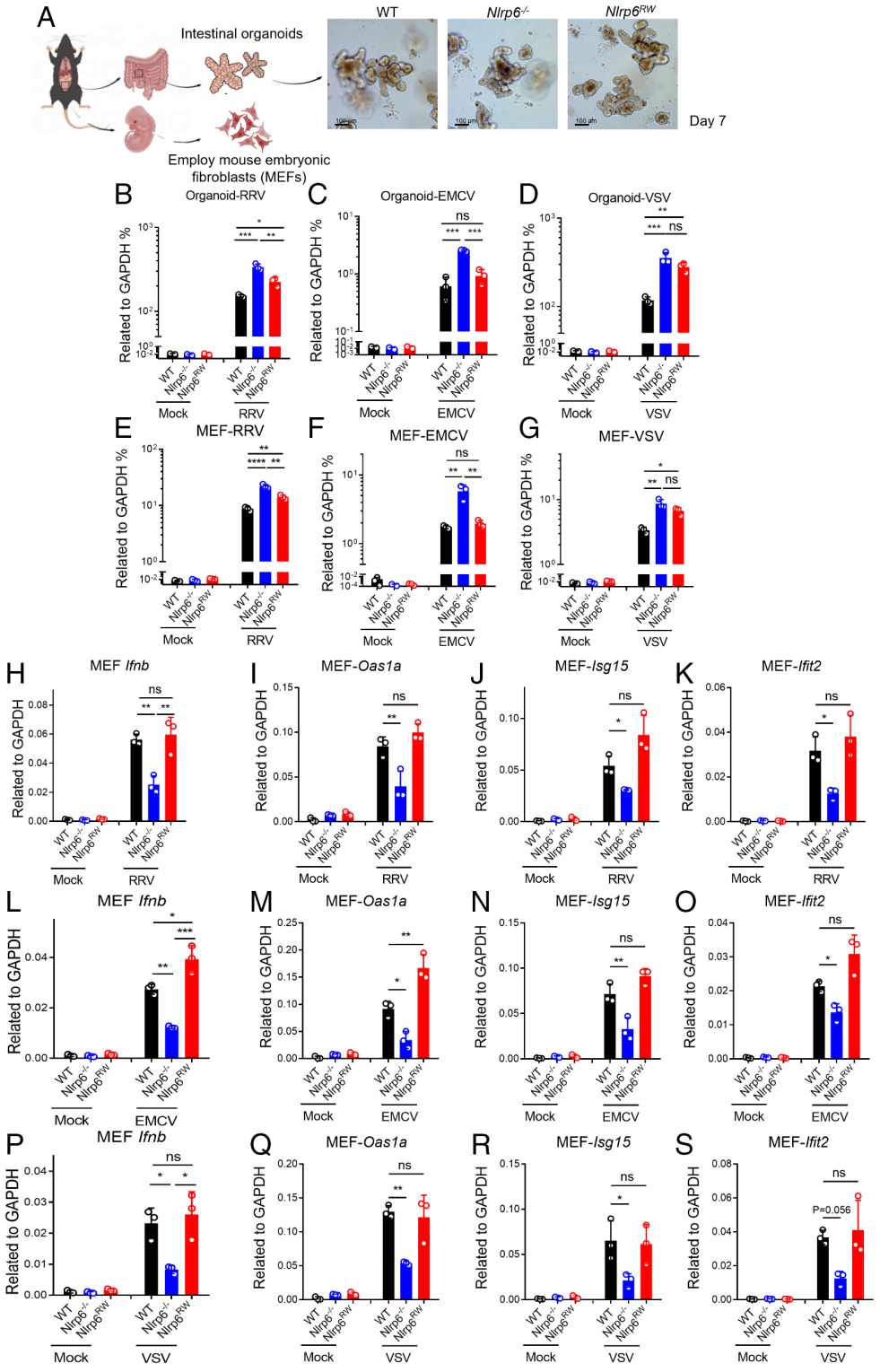

Fig. 4. Both NLRP6-mediated inflammasome activation and IFN-I production are important for the restriction of virus Infection in cells. (*A*) Isolation and culture of intestinal organoids and MEFs from WT, *Nlrp6*$^{-/-}$, and *Nlrp6*^{RW} mice. The morphology of the organoids on day 7 is shown. (Scale bar, 100 μm.) (*B–D*) Quantitative qRT-PCR analysis of corresponding viral load in intestinal organoids 12 h after RRV (*B*), EMCV (*C*), and VSV (*D*) infection. (*E–G*) Quantitative qRT-PCR analysis of corresponding viral load in MEFs 12 h after RRV (*E*), EMCV (*F*), and VSV (*G*) infection. (*H–K*) qRT-PCR analysis of *Ifnb* (*H*), *Oas1a* (*I*), *Isg15* (*J*), and *Ifit2* (*K*) mRNA in MEFs that were infected with RRV for 3 h. (*L–O*) qRT-PCR analysis of *Ifnb* (*L*), *Oas1a* (*M*), *Isg15* (*N*), and *Ifit2* (*O*) mRNA in MEFs that were infected with EMCV for 3 h. (*P–S*) qRT-PCR analysis of *Ifnb* (*P*), *Oas1a* (*Q*), *Isg15* (*R*), and *Ifit2* (*S*) mRNA in MEFs that were infected with VSV for 3 h. Data are representative of at least three independent experiments. The results are shown as mean ± SD. **P* < 0.05; ***P* < 0.01; ****P* < 0.001; *****P* < 0.0001; ns, not significant.

response to viral infection remained obscure. We utilized three representative RNA viruses to infect organoids and MEFs from *Nlrp6*$^{-/-}$, *Nlrp6*$^{R39E\&W50E}$, and WT mice. Interestingly, we found that two pathways mediated by NLRP6 exert distinct roles in antiviral immune responses to these three viruses (Fig. 4). First, Rotavirus (RV, a dsRNA virus) seems equally sensitive to NLRP6 inflammasome or NLRP6-induced interferon, previous studies indeed showed that RV can induce both inflammasome and

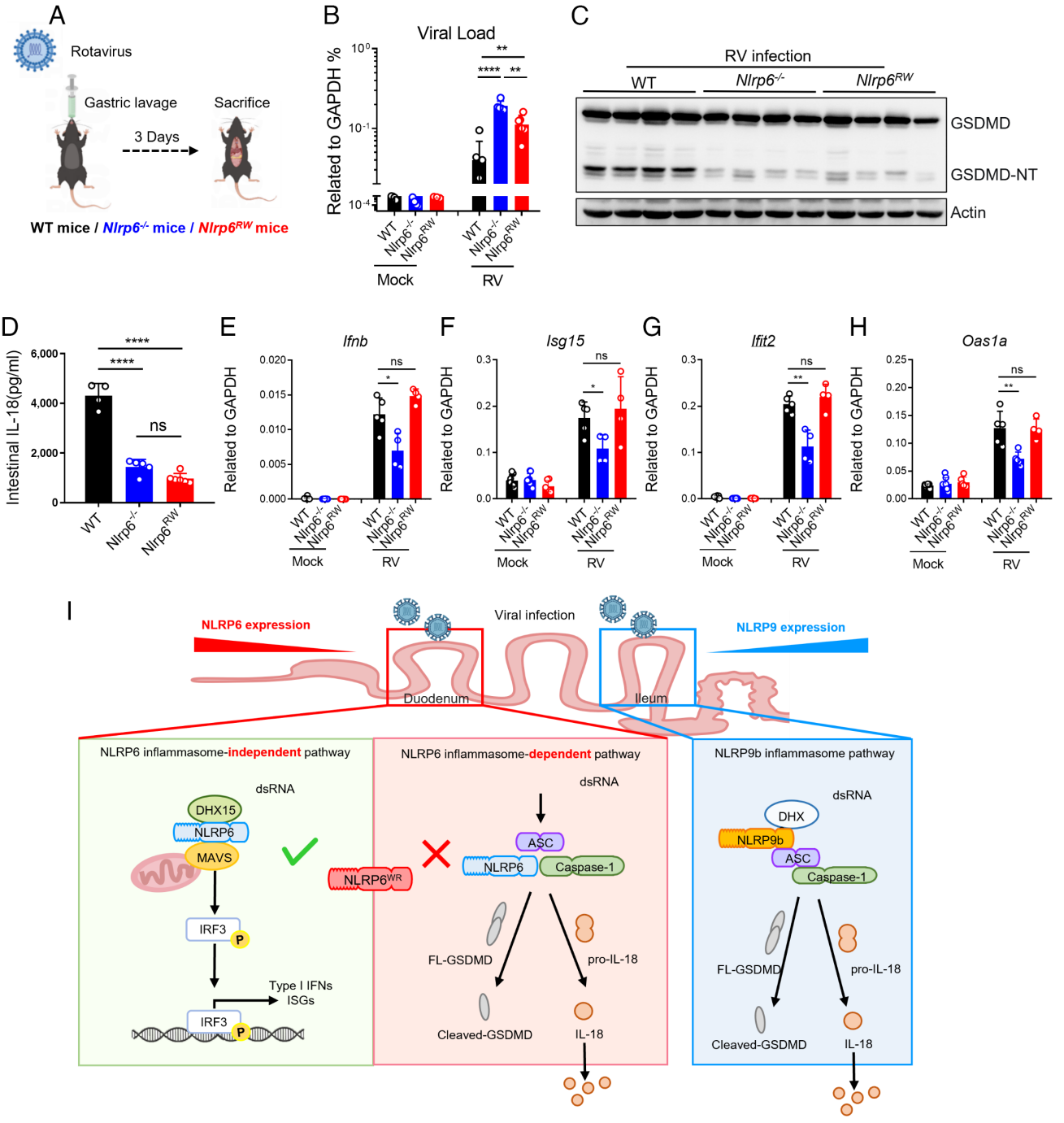

Fig. 5. The NLRP6^{RW} mutation suppresses NLRP6 inflammasome but not IFN-I pathway during enterovirus infection in vivo. (*A*) WT, *Nlrp6*$^{-/-}$, and *Nlrp6*^{RW} mice were orally inoculated by gavage with rotavirus and sacrificed 3 d later to collect samples for the following analysis. (*B*) Quantitative qRT-PCR analysis of viral load in proximal small intestine 3 d post rotavirus infection. (*C*) Immunoblot of cleaved GSDMD in jejunum tissues from WT, *Nlrp6*$^{-/-}$, and *Nlrp6*^{RW} mice at 3 d post rotavirus infection. (*D*) Intestine-explant supernatant IL-18 levels determined by ELISA from WT, *Nlrp6*$^{-/-}$, and *Nlrp6*^{RW} mice at 3 d post rotavirus infection. (*E–H*) qRT-PCR analysis of *Ifnb* (*E*), *Oas1a* (*F*), *Isg15* (*G*) and *Ifit2* (*H*) mRNA in jejunum tissues from WT, *Nlrp6*$^{-/-}$, and *Nlrp6*^{RW} mice at 24 h post rotavirus infection. (*I*) Mechanism of *Nlrp6*^{RW} mutant mouse model and synergistic antiviral effects of NLRP6 and NLRP9 in different segments of the intestine. Data are representative of at least three independent experiments. The results are shown as mean ± SD. **P* < 0.05; ***P* < 0.01; ****P* < 0.001; *****P* < 0.0001; ns, not significant.

interferon pathways (28, 29). Second, EMCV (a ss(+) RNA virus) is more sensitive to NLRP6-induced interferon. EMCV was shown to induce robust IFNb production both at the cellular level (29) and in vivo (10). Third, VSV (a ss(−) RNA virus) is more sensitive to NLRP6 inflammasome. The insensitivity of VSV to the IFN-I pathway may be attributed to the inhibition of the interferon response by VSV protein (29). The diverse downstream responses of NLRP6 triggered by different viruses may stem from the specific types of nucleic acids recognized directly or indirectly by NLRP6, leading to variations in the recruitment of downstream proteins. In addition, different RNA viruses may show distinct responsiveness to NLRP6-mediated pathways.

A previous study showed that mice with deficiency of components of the NLRP9 inflammasome, such as NLRP9b, ASC, CASP1, and GSDMD, exhibited susceptibility to rotaviral infection (28), suggesting that NLRP9b is also an important sensor for detecting rotavirus in the intestine (28). Notably, both NLRP9 and NLRP6 exert interesting expression pattern along the small

intestine—NLRP6 is high in proximal small intestine, while NLRP9b is high in distal small intestine (12). Considering that rotavirus infect proximal small intestine in the early time point and infect distal small intestine in late time point (30), NLRP6 and NLRP9b may cooperate in a space-time manner to defend against rotavirus. Moreover, since EMCV predominantly infects the proximal small intestine, the infection site aligns closely with the expression pattern of NLRP6 (10). Our work, in conjunction with prior studies, emphasizes the importance of NLRP6 inflammasome-independent functions in defending against EMCV infection. This is notably apparent in the intestine, the primary site of viral infection, where NLRs coordinate among each other with distinct expression patterns and downstream signals (31), creating a sophisticated defense system (Fig. 5*I*). Investigating whether these NLRs collaborate in defending against other microbes in the gut or contribute to additional physiological functions of the intestine is warranted.

In addition to the role of resisting enteroviruses, NLRP6 has also been shown to involve in the defense against hepatitis viruses within the liver (12). The rapid production of interferons (IFNs) and pro-inflammatory cytokines is a significant outcome of virus detection by NLRP6. Interferons play a crucial role in limiting viral replication, while inflammatory cytokines produced through inflammasome activation recruit immune cells to restrict infection but also contribute to tissue damage. Overall, our work offers a potential tool to distinguish the two pathways activated by viral infections, which may ultimately help control viral infections while minimizing the tissue damage.

Materials and Methods

Mice. The generation of *Nlrp6*$^{R39E\&W50E}$ mutant mice was achieved through CRISPR-Cas9 editing (32). Two selected gRNAs were ccacaagctagaggatgcgc and ggggcgactggagcgctc. The corresponding donor sequences were gcttatggctacactggaggagctgagccaggagcagctgaagcgcttccgccacaagctagaggatgcgcccctggatggccgcagcatcccggaggggcgactggagcgctcagacgctgtggaccttgtcgacaagctcattgagtt.

All mice were on the C57BL/6 background. Cohoused littermate mice were utilized as controls in the present study, and mice (aged 6 to 8 wk) were maintained on a strict 12-h light cycle under specific pathogen-free (SPF) conditions. All animal experiments were conducted following approval from the Ethics Committee of the University of Science and Technology of China.

Cell Culture. Immortalized BMDM, mouse embryonic fibroblasts (MEFs), HEK293T, and HEK293 cells were cultured in DMEM (HyClone) supplemented with 10% FBS (Viva Cell), penicillin (100 U/mL; Viva Cell), and streptomycin (100 mg/mL; Viva Cell). All cells were incubated at 37 °C in an atmosphere containing 5% CO_2.

Reagents and Antibodies. Primary antibodies were mouse anti-FLAG (F1804; Sigma–Aldrich), mouse anti-HA (M20003; Abmart), mouse anti-Actin (66009-1-Ig; ProteinTech), goat anti-NLRP6 (sc-50635, Santa Cruz Biotechnology), anti-ASC (67824; Cell Signaling Technology), anti-GSDMD (209845; Abcam), and mouse anti-Capase-1 (AG-20B-0042; Adipogen). The Mouse IL-18 enzyme-linked immunosorbent assay (ELISA) kit (Invivogen, 88-50618-88) and the CyQUANT™ LDH Cytotoxicity kit (ThermoFisher, C20300) were utilized for the experiments.

Isolation of Intestinal Organoids and MEFs. For isolation of intestinal organoids, small intestines were meticulously dissected, thoroughly rinsed with cold PBS, and then delicately opened longitudinally. Subsequently, they were incubated on ice in PBS containing EDTA (10 mM) for a duration of 30 to 45 min at 4 °C with gentle rotation. Subsequently, tissues were transferred to PBS. To separate crypts from connective tissue, a meticulous approach involving shaking or scraping was employed. The resulting mixture was then filtered through a 70-mm mesh into a 50-mL conical tube, ensuring the elimination of villus material and tissue fragments. The quantified isolated crypts were then embedded in 25 to 30 μL droplets of Matrigel™ (0.5×) at a concentration of 5 to 10 crypts per ml. These droplets were carefully plated onto a flat-bottom 48-well plate (Corning 3548) and allowed to solidify for 20 to 30 min in a 37 °C incubator. Following solidification, 300 μL of crypt culture medium were overlaid onto the Matrigel™, with regular changes every 3 d. The culture was meticulously maintained at 37 °C in fully humidified chambers containing 5% CO_2.

For isolation of MEFs, pregnant mice at 12.5 to 14.5 d of gestation are killed, and the uterus is exposed. The uterus is washed with PBS, and embryos with intact fetal membranes are collected. The fetal membranes are removed, and the embryos are washed with PBS. The head, internal organs, and limbs are removed from the embryos, and the remaining trunk is washed with PBS. The trunk is then cut into small fragments and digested with trypsin. After centrifugation, the pellet is resuspended in a culture medium and transferred to 10-cm dishes. The cells are cultured at 37 °C with 5% CO_2.

Cell Transfection. For transient transfection, mouse *Nlrp6* (NCBI accession #: NM_133946.2, NP_598707), human *Nlrp6* (NCBI accession #: NM_001276700, NP_001263629.1), mouse *Asc* (NCBI accession #: NM_023258.4, NP_075747.3), mouse *Gsdmd* (NCBI accession #: NM_026960, NP_081236), and mouse *Caspase-1* (NCBI accession #: NM_009807.2, NP_033937) were cloned into the pcDNA vector and transfected using PEI (23966-1; Polysciences).

For stable transfection, the genes encoding mouse *Nlrp6* and mouse *Asc* were inserted into the pLVX vector. The pLVX plasmids were efficiently co-transfected with Δ8.9 and vsvg viral packaging plasmids using PEI (23966-1; Polysciences). The subsequent viral particles were successfully generated in HEK293T cells. Then, HEK293 cells were strategically plated 12 h before the intended transduction in a 12-well plate, reaching a density of 2×10^5/mL. Over a 24-h period, viral media containing polybrene (1:1,000) were meticulously added to the cells. After this transduction period, the cells were expanded further in normal media, either for subsequent imaging procedures or for general propagation.

Immunoprecipitation and RNA-Binding Assays. After transfection, the 293 T cells were collected at 24 h using lysis buffer (containing 50 mM Tris-HCl, pH 7.4, 1% NP-40, 5% Glycerol, 1 mM EDTA, and 150 mM NaCl) supplemented with PMSF and complete protease inhibitors (Roche). The lysates were clarified by centrifugation (12,000 rpm), and the supernatants were incubated with M2 agarose beads (Sigma-Aldrich, A2220) for 4 h. Following six washes with the lysis buffer, the proteins bound to the M2 beads were released by 3× FLAG peptides (Sigma-Aldrich, F4799). In experiments involving protein–RNA interactions, 293 T cells were transfected with plasmid DNA and subsequently exposed to Encephalomyocarditis virus (EMCV) for an additional 24 h. FLAG-IP was performed on the cellular lysates, and the resulting 3× FLAG eluates were used for RNA extraction with Trizol (Tiangen, DP424). The isolated RNA was reverse-transcribed, and the expression levels of the EMCV D3 genes were quantified using SYBRGreen PCR (TAKARA, RR820A).

ASC Oligomerization Assay. At 24 h post-transfection, the 293 T cells were gently washed with ice-cold PBS and subsequently lysed in NP-40 at 4 °C for a duration of 30 min. After centrifugation at 12,000 rpm for 10 min at 4 °C, the resulting pellets underwent two washes with 1 mL of ice-cold PBS and then resuspended in 500 μL of PBS containing 2 mM disuccinimidyl suberate (ThermoFisher, 21655) for crosslinking at room temperature for half an hour. Subsequent to this treatment, the samples underwent centrifugation at 12,000 rpm for 10 min at 4 °C. The crosslinked pellets were then mixed in 40 μL of loading buffer and subjected to analysis via immunoblotting.

PI Staining. 293 T and iBMDM were grown on a 12-well plate to 1×10^5/mL. A 10 μg/mL working solution of PI in PBS was prepared. Live 293 T cells transfected with corresponding expression vectors were washed with PBS and incubated with the PI solution for 10 to 30 min at room temperature. Images were captured using an LSM880 confocal microscope.

ASC Speck Imaging. For ASC speck imaging, HEK293 cells stably coexpressing mouse ASC–mCherry and mouse NLRP6–GFP or its mutant were transfected. After 24 h of transfection, cells were treated with DAPI and imaged using a LSM880 laser scanning microscope with 20× objective.

Virus Infections. In virus infection experiments involving intestinal organoids and MEFs, RRV activation was achieved by treating it with trypsin (5 μg/mL) at 37 °C for 30 min before the actual infection process. Following this, the cells underwent thorough washing with ice-cold PBS three times and were subsequently

incubated with RRV, EMCV, or VSV at appropriate MOIs at 37 °C for 1 h. In the case of organoids, it was imperative to perform digestion and remove the Matrigel™ before initiating the infection. Once the RV inoculum was removed, cells were washed with PBS, cultured in serum-free medium (SFM), and then harvested for subsequent analysis using qPCR and western blot at the specified time points.

For rotavirus infection in vivo, mice (6 wk) were infected (i.g.) with 150% diarrhea dose (DD50) of EC virus in 200 μL sterile PBS (33). Mice were sacrificed, and small intestinal tissues were collected at indicated time points. Viral loads and ISG expression in intestinal tissues were detected by RT–qPCR.

Quantitative PCR. Total RNA was extracted from small intestine tissue, intestinal organoids, or MEFs using TRIzol reagent (Tiangen, DP424) and purified in accordance with the manufacturer's instructions. Subsequently, qPCR (SYBR premix EX Taq, Vazyme) was carried out using the CFX384 Real-Time System (Bio-Rad, 786BR04483) (34). The primer sequences for mRNA transcript detection are provided below:

RT-RV-F: GAGAATGTTCAAGACGTACTCCA
RT-RV-R: CTGTCATGGTGGTTTCAATTTC
RT-RRV NSP2-F: GAGAATCATCAGGACGTGCTT
RT-RRV NSP2-R: CGGTGGCAGTTGTTTCAAT
RT-EMCV-F: CCTCTTAATTCGACGCTTGAA
RT-EMCV-R: GGCAAGCATAGTGATCGAAG
RT-VSV-F: AGGGCACAGGGTTCAGAAGTAA
RT-VSV-R: GGAATCTGGCTGCAGCAAAG
RT-Gapdh-F: TGAGGCCGGTGCTGAGTATGTCG
RT-Gapdh-R: CCACAGTCTTCTGGGTGGCAGTG
RT-Ifit2-F: AGTACAACGAGTAAGGAGTCACT
RT- Ifit2-R: AGGCCAGTATGTTGCACATGG
RT- Ifnb1-F: TCCTGCTGTGCTTCTCCACCACA
RT-Ifnb1-R: AAGTCCGCCCTGTAGGTGAGGTT
RT-Isg15-F:GGTGTCCGTGACTAACTCCAT
RT- Isg15-R: TGGAAAGGGTAAGACCGTCCT
RT-Oas1a-F: GCCTGATCCCAGAATCTATGC
RT- Oas1a -R: GAGCAACTCTAGGGCGTACTG

The data obtained were analyzed using the Sequence Detection Software, following the ΔCt method as previously described (12). To normalize the data, the values were compared to the corresponding *Gapdh* values quantified in parallel amplification reactions.

Statistical Analysis. The animal experiments in current study were conducted based on our previous experience (35) and the sample size was determined accordingly. We included all animal results without using any randomization method. The bar graph data were presented as mean ± SD. Statistical analyses were performed using standard two-tailed unpaired Student's *t* test with GraphPad Prism 8.0.1. For comparing two nonparametric datasets, we employed a Mann–Whitney U test. We considered P values ≤ 0.05 as significant. The figure legends offer essential insights, detailing sample sizes, specifying biological replicates, outlining statistical tests, and summarizing main outcomes, ensuring clarity and comprehension of experimental results.

Data, Materials, and Software Availability. All study data are included in the article and/or *SI Appendix*.

ACKNOWLEDGMENTS. We thank Shuang Jia for maintaining some of the mouse colonies and Anlei Wang for plasmid construction. This work was supported by grants from the National Natural Science Foundation of China (82325025, 82341121) (S.Z.) and the CAS Project for Young Scientists in Basic Research (YSBR-074) (S.Z.).

Author affiliations: [a]Department of Digestive Disease, The First Affiliated Hospital of University of Science and Technology of China, Division of Life Sciences and Medicine, University of Science and Technology of China, Hefei 230001, China; [b]Institute of Immunology and the Chinese Academy of Sciences Key Laboratory of Innate Immunity and Chronic Disease, Division of Life Sciences and Medicine, University of Science and Technology of China, Hefei 230027, China; [c]Institute of Health and Medicine, Hefei Comprehensive National Science Center, Hefei 230051, China; [d]Department of Molecular Microbiology, Washington University School of Medicine, Saint Louis, MO 63110; [e]Division of Infectious Diseases, Department of Medicine, Washington University School of Medicine, Saint Louis, MO 63110; [f]Department of Biological Chemistry and Molecular Pharmacology, Harvard Medical School, Boston, MA 02115; and [g]Program in Cellular and Molecular Medicine, Boston Children's Hospital, Boston, MA 02115

1. D. Li, M. Wu, Pattern recognition receptors in health and diseases. *Signal Transduct. Target. Ther.* **6**, 291 (2021).
2. G. Chen, M. H. Shaw, Y.-G. Kim, G. Nuñez, NOD-like receptors: Role in innate immunity and inflammatory disease. *Annu. Rev. Pathol. Mech. Dis.* **4**, 365–398 (2009).
3. L. Ghimire, S. Paudel, L. Jin, S. Jeyaseelan, The NLRP6 inflammasome in health and disease. *Mucosal Immunol.* **13**, 388–398 (2020).
4. J. Henao-Mejia, E. Elinav, C. A. Thaiss, R. A. Flavell, Inflammasomes and metabolic disease. *Annu. Rev. Physiol.* **76**, 57–78 (2014).
5. S. Normand *et al.*, Nod-like receptor pyrin domain-containing protein 6 (NLRP6) controls epithelial self-renewal and colorectal carcinogenesis upon injury. *Proc. Natl. Acad. Sci. U.S.A.* **108**, 9601–9606 (2011).
6. E. Elinav *et al.*, NLRP6 inflammasome regulates colonic microbial ecology and risk for colitis. *Cell* **145**, 745–757 (2011).
7. M. Wlodarska *et al.*, NLRP6 inflammasome orchestrates the colonic host–microbial interface by regulating goblet cell mucus secretion. *Cell* **156**, 1045–1059 (2014).
8. H. Hara *et al.*, The NLRP6 inflammasome recognizes lipoteichoic acid and regulates Gram-positive pathogen infection. *Cell* **175**, 1651–1664.e1614 (2018).
9. M. Levy *et al.*, Microbiota-modulated metabolites shape the intestinal microenvironment by regulating NLRP6 inflammasome signaling. *Cell* **163**, 1428–1443 (2015).
10. P. Wang *et al.*, Nlrp6 regulates intestinal antiviral innate immunity. *Science* **350**, 826–830 (2015).
11. P. K. Anand *et al.*, NLRP6 negatively regulates innate immunity and host defence against bacterial pathogens. *Nature* **488**, 389–393 (2012).
12. C. Shen *et al.*, Phase separation drives RNA virus-induced activation of the NLRP6 inflammasome. *Cell* **184**, 5759–5774.e5720 (2021).
13. Z. Hu *et al.*, Crystal structure of NLRC4 reveals its autoinhibition mechanism. *Science* **341**, 172–175 (2013).
14. C. Shen *et al.*, Molecular mechanism for NLRP6 inflammasome assembly and activation. *Proc. Natl. Acad. Sci. U.S.A.* **116**, 2052–2057 (2019).
15. A. Lu *et al.*, Unified polymerization mechanism for the assembly of ASC-dependent inflammasomes. *Cell* **156**, 1193–1206 (2014).
16. M. Levy, H. Shapiro, C. A. Thaiss, E. Elinav, NLRP6: A multifaceted innate immune sensor. *Trends Immunol.* **38**, 248–260 (2017).
17. U. Ohto, Activation and regulation mechanisms of NOD-like receptors based on structural biology. *Front. Immunol.* **13**, 953530 (2022).
18. H. Guo, S. A. Gibson, J. P. Y. Ting, Gut microbiota, NLR proteins, and intestinal homeostasis. *J. Exp. Med.* **217**, e20181832 (2020).
19. L. Ghimire *et al.*, NLRP6 negatively regulates pulmonary host defense in Gram-positive bacterial infection through modulating neutrophil recruitment and function. *PLoS Pathog.* **14**, e1007308 (2018).
20. V. G. Magupalli *et al.*, HDAC6 mediates an aggresome-like mechanism for NLRP3 and pyrin inflammasome activation. *Science* **369**, eaas8995 (2020).
21. Z. Shi *et al.*, Segmented filamentous bacteria prevent and cure rotavirus infection. *Cell* **179**, 644–658.e613 (2019).
22. R. Li, S. Zhu, NLRP6 inflammasome. *Mol. Aspects Med.* **76**, 100859 (2020).
23. R. Li, Y. Zan, K. Sui, S. Zhu, The latest breakthrough on NLRP6 inflammasome. *Precis. Clin. Med.* **5**, pbac022 (2022).
24. M. Carty, C. Guy, A. G. Bowie, Detection of viral infections by innate immunity. *Biochem. Pharmacol.* **183**, 114316 (2021).
25. X. Ren *et al.*, Nucleic DHX9 cooperates with STAT1 to transcribe interferon-stimulated genes. *Sci. Adv.* **9**, eadd5005 (2023).
26. J. W. Schoggins, Interferon-stimulated genes: What do they all do? *Annu. Rev. Virol.* **6**, 567–584 (2019).
27. R. Medzhitov, Toll-like receptors and innate immunity. *Nat. Rev. Immunol.* **1**, 135–145 (2001).
28. S. Zhu *et al.*, Nlrp9b inflammasome restricts rotavirus infection in intestinal epithelial cells. *Nature* **546**, 667–670 (2017).
29. H. Kato *et al.*, Differential roles of MDA5 and RIG-I helicases in the recognition of RNA viruses. *Nature* **441**, 101–105 (2006).
30. W. G. Starkey *et al.*, Kinetics, tissue specificity and pathological changes in murine rotavirus infection of mice. *J. General Virol.* **67**, 2625–2634 (1986).
31. T. Wan, Y. Wang, K. He, S. Zhu, Microbial sensing in the intestine. *Protein Cell* **14**, 824–860 (2023).
32. Y. Wang *et al.*, The RNA helicase Dhx15 mediates Wnt-induced antimicrobial protein expression in Paneth cells. *Proc. Natl. Acad. Sci. U.S.A.* **118**, e2017432118 (2021).
33. A. Wang *et al.*, m6A modifications regulate intestinal immunity and rotavirus infection. *eLife* **11**, e73628 (2022).
34. K. He *et al.*, Gasdermin D licenses MHCII induction to maintain food tolerance in small intestine. *Cell* **186**, 3033–3048.e3020 (2023).
35. G. Zhang *et al.*, Glucosylated nanoparticles for the oral delivery of antibiotics to the proximal small intestine protect mice from gut dysbiosis. *Nat. Biomed. Eng.* **6**, 867–881 (2022).